A Simple Reluctance Calibration Strategy to Obtain the Flux-Linkage Characteristics of Switched Reluctance Machines

Lefei Ge, *Student Member, IEEE*, Iliya Ralev, Annegret Klein-Hessling, *Student Member, IEEE*, Shoujun Song, *Senior Member, IEEE*, and Rik W. De Doncker, *Fellow, IEEE*

***Abstract*—To predict the dynamic performance or realize advanced control for switched reluctance machines (SRMs), knowledge of the flux-linkage characteristics is essential. These characteristics can be determined by a magnetic equivalent circuit (MEC), a finite-element method (FEM), or measurements. The MEC and FEM results are usually not accurate, while results from measurements are accurate, but very expensive and time-consuming. In this paper, a new calibration strategy is proposed to quickly obtain flux-linkage characteristics with low effort. First, flux-linkage samples at aligned and unaligned positions are obtained from fast measurement. Then, a reluctance calibration strategy is utilized to calibrate the airgap and iron reluctance parameters with measurement values. The calibration results are compared with complete measurement results, and good agreements can be found, which verifies the feasibility and accuracy of the proposed strategy. Furthermore, a simulation model is built in MATLAB with the calibration results, and dynamic performances at different speeds and control strategies are simulated and compared with experiments for further validation. In addition, the applicability of the proposed method to the variation of some parameters, such as material, airgap, and winding placement, and different topologies is discussed as well. The presented strategy can serve as a low-effort way to obtain accurate flux-linkage characteristics of SRMs.**

***Index Terms*—Finite-element method (FEM), flux-linkage characteristics, measurement, modeling, switched reluctance machine (SRM).**

I. Introduction

SWITCHED reluctance machines (SRMs) have been attracting more and more attention from researchers and industry due to their low cost and performance advantages such as simple and rugged structure, wide speed range, and high temperature endurance [1], [2]. Especially, in recent years, the growing price of rare-earth permanent magnets has made the cost advantage more prominent [3].

The flux-linkage characteristics are very critical for the performance prediction [4] and advanced control of the SRMs [5]. Several methods have been proposed to obtain the flux-linkage characteristics of SRMs, which can be mainly divided into three categories: magnetic equivalent circuit (MEC), finite-element method (FEM), and measurement. The MEC approach can determine the flux-linkage profile quickly, but its accuracy heavily depends on assumptions and simplifications. The FEM is more accurate than the MEC due to finer magnetic section division. However, it does not consider the changes of material properties and geometries during the process of manufacturing [6]. To more accurately obtain the flux-linkage characteristics of SRMs, the measurement method is preferred.

There are mainly two kinds of experimental measurement methods, namely, direct methods and indirect methods. The direct methods employ a flux sensor placed on a stator pole to measure flux [7]. Due to installation difficulties and unsatisfactory accuracy caused by leakage flux, this direct method is seldom used. In the indirect methods, an ac power supply [8] or a dc pulse current [6], [9] is applied to excite the phase winding, and the phase voltage and current are recorded to calculate the flux linkage. The ac excitation methods can eliminate the residual flux of the core material to achieve higher measurement accuracy, but they need an extra sinusoidal voltage source. The dc excitation methods only employ a standard machine converter and can also obtain satisfactory measurement results, which makes these methods more popular.

Traditional indirect methods require rotor clamping devices to fix the rotor to a certain position during the measurement process, which increases the complexity and cost. More importantly, rotor clamping is not applicable if SRMs are already in service. Recently, some measurement methods without rotor clamping devices are reported. In [10], a stationary test and rotary test combined measurement method is presented. The stationary test determines the flux linkage at the aligned position, while the rotary test measures flux linkage under different current levels when the machine is driven at low and nearly constant speed. The final flux-linkage characteristics are obtained by fitting the

Manuscript received November 22, 2018; revised February 15, 2019 and May 2, 2019; accepted June 13, 2019. Date of publication June 27, 2019; date of current version December 13, 2019. The work of L. Ge was supported by the China Scholarship Council (CSC). Recommended for publication by Associate Editor A. Muetze. *(Corresponding author: Lefei Ge.)*

L. Ge, I. Ralev, A. Klein-Hessling, and R. W. De Doncker are with the Institute for Power Electronics and Electrical Drives, RWTH Aachen University, 52066 Aachen, Germany (e-mail: Lefei.Ge@isea.rwth-aachen.de; Iliya.Ralev@isea.rwth-aachen.de; akh@isea.rwth-aachen.de; post@isea.rwth-aachen.de).

S. Song is with the School of Automation, Northwestern Polytechnical University, Xi'an 710072, China (e-mail: sunnyway@nwpu.edu.cn).

Color versions of one or more of the figures in this paper are available online at http://ieeexplore.ieee.org.

Digital Object Identifier 10.1109/TPEL.2019.2925656

rotary test results to stationary test results at the aligned position. This method only requires a standard drive test bench and can be performed faster than traditional indirect methods. However, it is still time-consuming to obtain the entire flux-linkage characteristics completely by the described measurement approach. In [11], flux-linkage characteristics at unaligned position, mid position, and aligned position are obtained by simultaneously exciting all phases at one phase-aligned position for a four-phase 8/6-pole SRM. Then, a second-order Fourier series is used to obtain all the flux-linkage characteristics. This method is fast and convenient, but the accuracy of measurement is reduced because of mutual inductances. Besides, the second-order Fourier series model exhibits inherent errors especially in the magnetic saturation area. In [12] and [13], a torque-balanced measurement approach is proposed to measure four position flux-linkage characteristics for a three-phase 12/8 machine. However, the measurement accuracy of flux-linkage characteristics at 15° position is affected by excitation forms. In long flux path excitation form, measurement errors are quite significant. In [14], an analytical model is proposed based on scaling of reluctance characteristics to describe the relationship among rotor position, reluctance, and phase current. Flux-linkage characteristics at four positions or two positions obtained from torque-balanced measurement are employed to calibrate the analytical model. The four-position method can achieve a good accuracy, but its measurements are somewhat complicated, while the two-position method is less accurate.

In this paper, a new indirect method for flux-linkage acquisition for the SRM is proposed. Based on measured flux-linkage characteristics at aligned and unaligned positions, a reluctance calibration strategy is proposed to calibrate FEM simulation results. With low-effort calibration, results can be good enough to predict dynamic performance and control of the machine. Compared with the existing literature research efforts, the proposed method has the following features.

1) Compared with the rotor clamping method, the proposed method eliminates the rotor clamping devices, which effectively reduces the time for design, construction, and testing of the measurement platform.
2) Compared with the methods that obtain the entire flux-linkage characteristics only by measurement, the proposed method only needs to measure the flux-linkage data at two rotor positions, which reduces the experimental effort.
3) Compared with the FEM simulations, the proposed method has a better accuracy and is robust to parameter variations.

The rest of this paper is organized as follows. The measurements of flux-linkage characteristics at aligned and unaligned positions are described in Section II. Section III presents the proposed reluctance calibrated method with detailed analysis and preliminary verification. In Section IV, the effectiveness of the method is further verified through the static and dynamic experiments with a three-phase 18/12-pole SRM prototype. Section V discusses the robustness of the proposed method with the variation of several uncertain factors and the applicability to different topologies. Section VI concludes this paper.

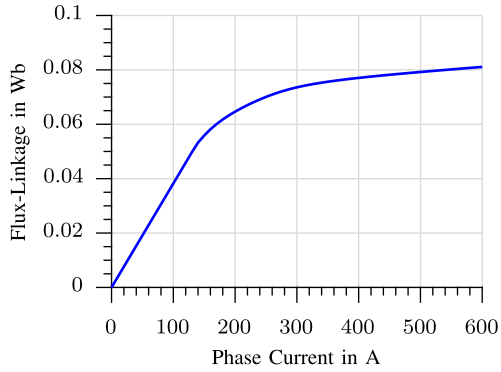

Fig. 1. Measured flux-linkage characteristic of the SRM prototype at the aligned position.

II. Measurement of Flux-Linkage Characteristics at Aligned and Unaligned Positions

Among all the flux-linkage characteristics, flux-linkage characteristics at aligned and unaligned positions are the most important, which determines the average torque output capability. They are measured in this paper without rotor clamping devices. The measurement is implemented on a three-phase 18/12 SRM prototype. It is a 35-kW machine for a small electric car [15]. More specific data can refer to SRM1 in Table I in the appendix.

A. Flux Linkage at the Aligned Position

The measurement of flux linkage at the aligned position of the SRM prototype has been presented in [10]. It is briefly concluded in this paper as the following processes.

1) A high-current pulse, e.g., rated current, for a few seconds is applied to one phase of the machine to make it rotate to the aligned position.
2) A pulsed dc voltage is simultaneously applied to one phase, and the phase current and phase voltage are recorded by a digital storage oscilloscope.
3) Based on the recorded phase voltage and current data, the flux linkage can be calculated as

$$\psi(i) = \int_0^t (u(t) - Ri(t))dt \tag{1}$$

where t is the sample time and ψ, u, i, and R are the phase flux linkage, voltage, current, and resistance, respectively.
4) The final flux-linkage trajectory can be plotted upon phase current, as shown in Fig. 1.

B. Flux Linkage at the Unaligned Position

Although the flux linkage at the unaligned position can be measured by the torque-balanced method proposed in [12] and [13], a more convenient way is to calculate the unaligned inductance from dynamic current waveform.

The phase voltage equation of an SRM can be written as

$$u = Ri + L\frac{di}{dt} + i\omega\frac{dL}{d\theta} \tag{2}$$

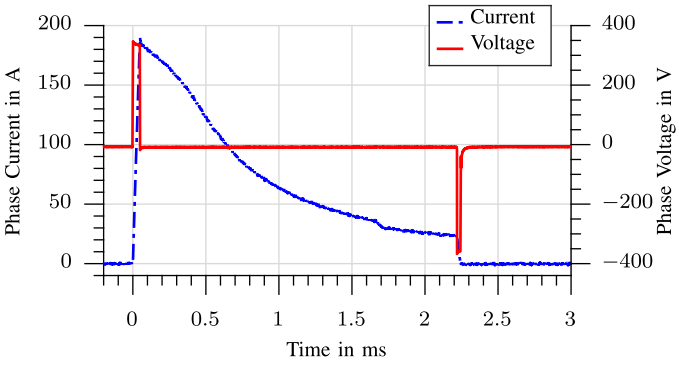

Fig. 2. Measured current and voltage waveforms under the single-pulse control mode.

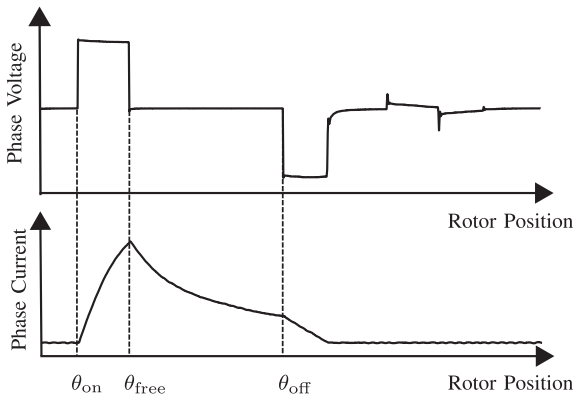

Fig. 3. Schematic diagram of dynamic waveform with θ_{free} under single-pulse control.

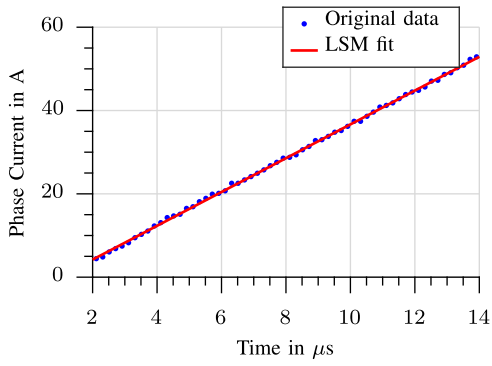

Fig. 4. Curve-fitting result with the LSM.

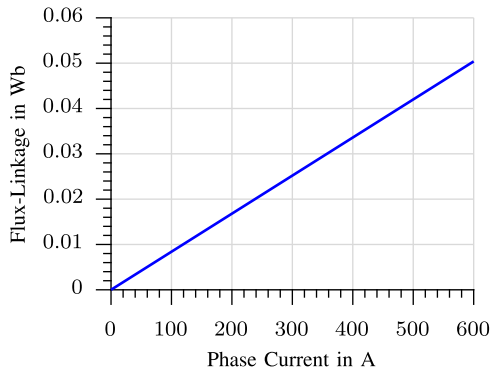

Fig. 5. Measured flux-linkage characteristics of the SRM prototype at the unaligned position.

where L is the phase inductance and ω and θ are the machine rotor angular speed and position, respectively.

At the unaligned position and low speed, the back electromotive force (back EMF) of the machine $i\omega dL/d\theta$ can be eliminated from (2). Hence, the inductance at unaligned position can be deduced as

$$L = \frac{u - Ri}{\frac{di}{dt}}. \tag{3}$$

Fig. 2 shows the measured current and voltage waveforms with turn-ON angle $\theta_{on} = 0$ °el, freewheeling angle $\theta_{free} = 3.5$ °el, and turn-OFF angle $\theta_{off} = 160$ °el at 1000 r/min. The SRM works as a motor under the single-pulse control mode. θ_{free} is adjusted to achieve the targeted speed. The definition of θ_{free} can refer to Fig. 3. It is the angle where the phase voltage begins to drop zero. In this case, the positive phase excitation only lasts 3.5 °el, which is very narrow. The narrow excitation has two benefits: 1) there is no overlap between different phase excitations, so the mutual coupling could be avoided; and 2) the magnitude of the phase current is also limited, which can reduce the copper loss. Similar to the measurement at the aligned position, the narrow excitation and low speed operation also cause small temperature rise. Therefore, the phase resistance is near to the value measured at the aligned position. The current change rate di/dt can be estimated with the least squares method (LSM), which is given as

$$\frac{di}{dt} = \frac{\sum_{k=1}^{n}(t_k - \frac{1}{n}\sum_{k=1}^{n} t_k)(i_k - \frac{1}{n}\sum_{k=1}^{n} i_k)}{\sum_{k=1}^{n}(t_k - \frac{1}{n}\sum_{k=1}^{n} t_k)^2} \tag{4}$$

where t_k and i_k are the instantaneous time and current, respectively, and n is the number of samples.

The curve-fitting result with the LSM is presented in Fig. 4. The curve fitting begins at 2 μs when the voltage rises to the nominated value and ends at 14 μs where the rotor position is about 1 °el with the sampling interval 0.2 μs. The di/dt in Fig. 4 is calculated to be 4057.2 A/ms. Then, the inductance at unaligned position L_u can be obtained by (3), and it is 0.084 mH. Assuming no saturation at the unaligned position, the flux-linkage trajectory at the unaligned position can be plotted with L_u, which is shown in Fig. 5.

III. Reluctance Calibration Strategy

The flux-linkage characteristics obtained by the two-dimensional (2-D) FEM analysis and measurement in Section II are compared in Fig. 6. It can be found that the errors occur at both aligned and unaligned positions. Before magnetic saturation, the FEM curve is up to 20% higher than the measured one at the aligned position, while it is about 5% lower at the unaligned position. The errors of flux linkage between the FEM and the

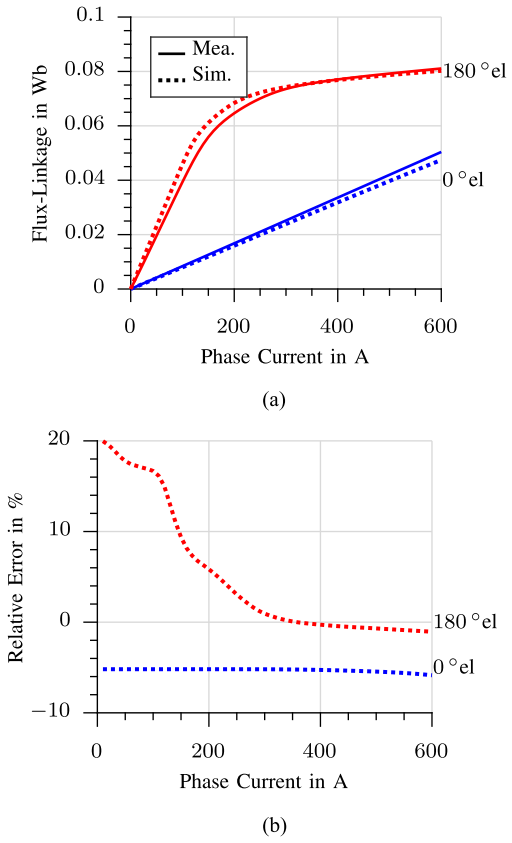

Fig. 6. Flux-linkage characteristics of the SRM prototype obtained by the 2-D FEM with NO20. (a) Flux-linkage characteristics. (b) Relative errors.

measurement can be owed to the inaccurate of reluctance characteristics. To obtain more accurate flux-linkage characteristics, a reluctance calibration strategy is proposed in this section.

A. Basic Reluctance Theory in SRMs

According to the MEC, the reluctance of the SRM R can be defined as the ratio of the magnetic motive force Θ and the magnetic flux ϕ. Based on the electromagnetic theory, Θ and ϕ can be derived from the phase current and flux linkage, respectively. Hence, reluctance can be obtained from flux-linkage characteristics, which is given as

$$R = \frac{\Theta}{\phi} = \frac{N^2 I}{\psi} \tag{5}$$

where N is the number of turns.

More specifically, the reluctance of the SRM consists of two parts: airgap reluctance and iron core reluctance. The airgap reluctance R_{g} corresponds to the airgap between the stator and rotor poles, and it can be calculated from the airgap inductance as

$$R_{\mathrm{g}} = \frac{N^2}{L_{\mathrm{g}}} \tag{6}$$

where L_{g} is the airgap inductance, which is approximately equal to the machine unsaturated inductance.

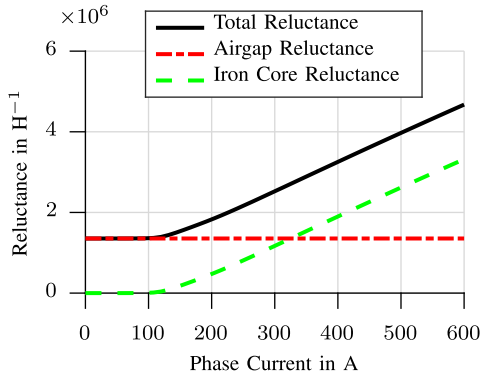

Fig. 7. Reluctance separation at the aligned position.

R_{g} can also be estimated from the geometry parameters as

$$R_{\mathrm{g}} = \frac{l_{\mathrm{g}}}{\mu_0 S} \tag{7}$$

where l_{g}, μ_0, and S denote the mean effective length of airgap, the air magnetic permeability, and the cross-sectional area, respectively.

Iron core reluctance R_{i} corresponds to the stator and rotor ferromagnetic poles and yokes. It can be either calculated by subtracting R_{g} from the whole reluctance R or by magnetic circuit equation (8), as

$$R_{\mathrm{i}} = \frac{l_{\mathrm{i}}}{\mu_0 \mu_{\mathrm{r}} S} \tag{8}$$

where l_{i} and μ_{r} denote average flux path in the ferromagnetic material and relative permeability of ferromagnetic material, respectively.

Before magnetic saturation, the relative permeability of ferromagnetic material μ_{r} is very large. R_{i} is usually neglected to facilitate calculating R_{g}. After magnetic saturation, μ_{r} reduces quickly with the increase of phase current. Therefore, the iron core reluctance R_{i} cannot be neglected any more, and it can be separated by subtracting R_{g} from the total reluctance R.

As an example, Fig. 7 shows the separation of airgap and iron core reluctance at the aligned position. The total reluctance in Fig. 7 (black curve) can be calculated from the simulated flux-linkage characteristics with (5). With the analytical method in [16], the airgap and unsaturated iron core reluctance can be estimated, which are $1.43\mathrm{e}6H^{-1}$ and $2.99\mathrm{e}4H^{-1}$, respectively. The unsaturated iron core reluctance is only about 2% of the airgap reluctance. Therefore, it is reasonable to neglect the iron core reluctance before saturation. The airgap reluctance (red curve) will not vary with the phase current. By subtracting the airgap reluctance from the total reluctance, it is easy to obtain the iron core reluctance (green curve). Similarly, the airgap and iron core reluctance at other positions can also be obtained by neglecting the unsaturated iron core reluctance.

B. Airgap Reluctance Calibration

The airgap inductance is widely known as a nonlinear function of rotor position θ, and it will not change with the variation of

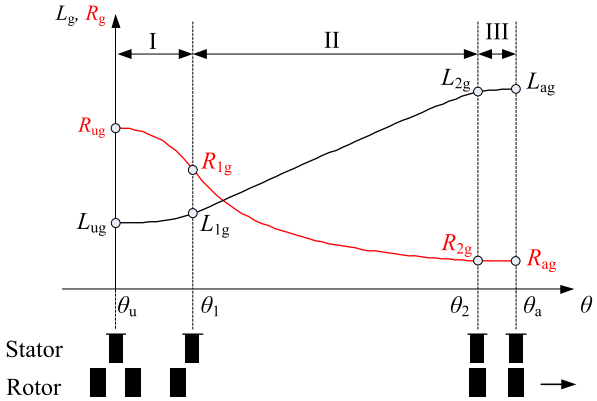

Fig. 8. Airgap inductance and reluctance as function of rotor position.

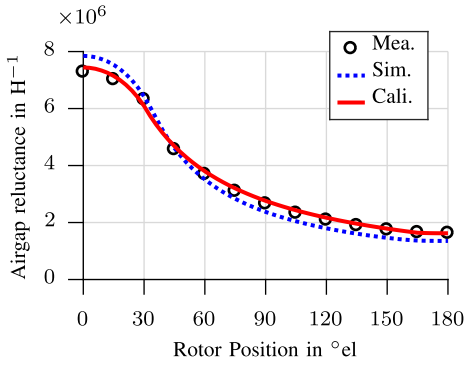

Fig. 9. Airgap reluctance comparison of the SRM prototype with the measured, original FEM, and calibrated data.

the phase current i. A typical curve of airgap inductance and reluctance in one electric period is given in Fig. 8. In this figure, θ_u is the unaligned position, θ_a is the aligned position, θ_1 is the position where the rotor pole and the stator pole begin to overlap, θ_2 is the position where the back edge of the rotor pole and stator pole begin to overlap, and L_{ug}, L_{1g}, L_{2g}, and L_{ag} are the inductance values at θ_u, θ_1, θ_2, and θ_a, respectively. R_{ug}, R_{1g}, R_{2g}, and R_{ag} are the corresponding reluctance. θ_1 and θ_2 can be calculated by the following equations [17]:

$$\theta_1 = \theta_a - \frac{\beta_r + \beta_s}{2} \tag{9}$$

$$\theta_2 = \theta_a - \frac{\beta_r - \beta_s}{2} \tag{10}$$

where β_s and β_r are the pole arc of the stator and rotor, respectively.

As can be seen in Fig. 8, the inductance curve consists of two nonlinear regions that are connected through a linear curve. The inductance between θ_1 and θ_2 can be expressed as

$$\begin{aligned} L_g(\theta) &= \frac{L_{1g} - L_{2g}}{\theta_1 - \theta_2}(\theta - \theta_1) + L_{1g} \\ &= \frac{L_{1g} - L_{2g}}{\theta_1 - \theta_2}\theta + \frac{L_{1g}\theta_2 - L_{2g}\theta_1}{\theta_2 - \theta_1}. \end{aligned} \tag{11}$$

Substituting (7) into (11) gives

$$\begin{aligned} \frac{N^2}{R_g(\theta)} &= \frac{\frac{N^2}{R_{1g}} - \frac{N^2}{R_{2g}}}{\theta_1 - \theta_2}\theta + \frac{\frac{N^2}{R_{1g}}\theta_2 - \frac{N^2}{R_{2g}}\theta_1}{\theta_2 - \theta_1} \\ &= N^2\left(\frac{R_{1g} - R_{2g}}{R_{1g}R_{2g}(\theta_2 - \theta_1)}\theta + \frac{R_{2g}\theta_2 - R_{1g}\theta_1}{R_{1g}R_{2g}(\theta_2 - \theta_1)}\right). \end{aligned} \tag{12}$$

Let

$$a = \frac{R_{1g} - R_{2g}}{R_{1g}R_{2g}(\theta_2 - \theta_1)} \tag{13}$$

$$h = \frac{R_{2g}\theta_2 - R_{1g}\theta_1}{R_{1g}R_{2g}(\theta_2 - \theta_1)}. \tag{14}$$

Then, the airgap reluctance can be represented as

$$R_g(\theta) = \frac{1}{a\theta + h}\ (\theta_1 \le \theta \le \theta_2). \tag{15}$$

From (7), it can be seen that R_g is determined by l_g and S. In the process of manufacturing, the area of machine poles can be guaranteed, and it will not differ a lot. Thus, S will keep constant. However, the airgap length usually has a relatively significant variation compared to S. Thus, in this paper, S between FEM simulation and measurement results is assumed to be the same, and we assume that the error of reluctance comes from l_g. In this paper, the ratio between $l_{g,mea}$ and $l_{g,sim}$ is assumed to be constant in regions I and III; then, the measured airgap reluctance at unaligned and aligned positions can be used to calibrate the reluctance in these two regions, respectively. The formula is shown as

$$R_{g,Cali.}(\theta) = \frac{R_{ug,Mea.}}{R_{ug,Sim.}}R_{g,Sim.}, \theta_u \le \theta \le \theta_1 \tag{16}$$

$$R_{g,Cali.}(\theta) = \frac{R_{ag,Mea.}}{R_{ag,Sim.}}R_{g,Sim.}, \theta_2 \le \theta \le \theta_a \tag{17}$$

where $R_{g,Sim.}$, $R_{g,Mea.}$, and $R_{g,Cali.}$ are FEM simulated, measured, and calibrated reluctance, respectively. $R_{ug,Mea.}$, $R_{ug,Sim.}$, $R_{ag,Mea.}$, and $R_{ag,Sim.}$ are the corresponding values at θ_u and θ_a, respectively.

Fig. 9 presents the airgap reluctance curves of the SRM prototype with the measured, original FEM simulated, and calibrated data. The measured data are from the measurement in [10]. From this figure, we can see that the errors between the measurement and the FEM can be effectively reduced by the proposed calibration method, which preliminary proves the validity of the proposed airgap reluctance calibration method.

C. Iron Core Reluctance Calibration

Differently from R_g, R_i will also change along with the variation of phase current due to magnetic saturation[14]. It is a nonlinear function of both the rotor position and the phase current, and the typical curve of iron reluctance can refer to the FEM simulation results (solid line) in Fig. 10.

From (8), it can be seen that R_i is determined by l_i, S_i, and μ_r. The l_i and S_i depend on machine geometry parameters. A

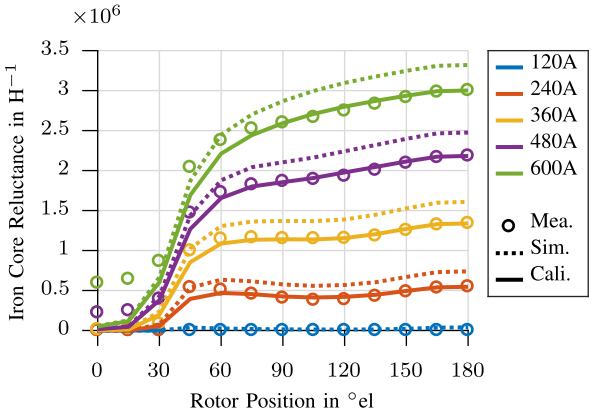

Fig. 10. Iron reluctance comparison of the SRM prototype with the measured, original FEM, and calibrated data.

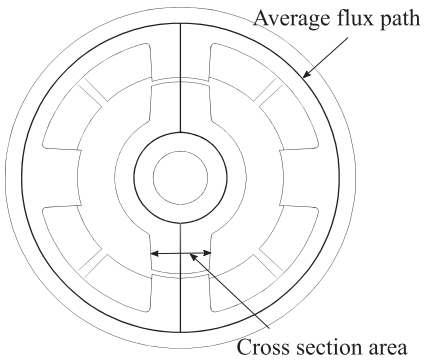

Fig. 11. Simplified flux path of a two-phase 4/2 pole SRM.

simplified model of flux path in ferromagnetic material at the aligned position is shown in Fig. 11 [18]. As seen in this figure, these linked geometry parameters are main indexes of machine design, which can be guaranteed by manufactures to be within certain limits. However, the electromagnetic properties of electrical steel usually change during the manufacturing process of electrical machines [12]. Thus, μ_{r} should be calibrated. At the aligned position, it can be calibrated by

$$\mu_{\mathrm{r,Cali}} = \frac{R_{\mathrm{ai,Sim}}}{R_{\mathrm{ai,Mea}}}\mu_{\mathrm{r}} \tag{18}$$

where $R_{\mathrm{ai,Sim}}$ and $R_{\mathrm{ai,Mea}}$ are simulated and measured iron reluctance at θ_{a}, respectively. $\mu_{\mathrm{r,Cali}}$ is the calibrated relative permeability.

To simplify the analysis, μ_{r} is assumed to be independent with the rotor position, and it only depends on the phase current. Based on this assumption, the simulated iron reluctance can be calibrated by

$$R_{\mathrm{i,Cali}}(\theta) = \frac{\mu_{\mathrm{r}}}{\mu_{\mathrm{r,Cali}}}R_{\mathrm{i,Sim}}(\theta) = \frac{R_{\mathrm{ai,Mea}}}{R_{\mathrm{ai,Sim}}}R_{\mathrm{i,Sim}}(\theta). \tag{19}$$

Fig. 10 compares the iron core reluctance curves of the SRM prototype with the measured, original FEM simulated, and calibrated data. It can be seen that good agreements can be found after 60 °el. The error is relatively big before 30 °el. These errors may be caused by measurement errors at the unaligned position in [10]. Besides, the assumption that μ_{r} is independent with

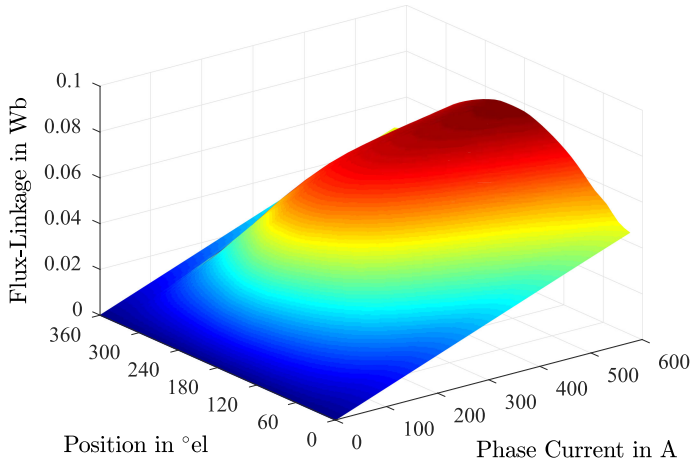

Fig. 12. Entire flux-linkage characteristics from the proposed method.

rotor position will also cause errors at low position area because the saturation degree quite differs with that at the aligned position. It should be noted that these errors at low position area will not cause too big error in the final calculation of flux linkage. This is mainly because the iron reluctance in this region is much smaller than the airgap reluctance, which can be easily seen by comparing Figs. 9 and 10.

After obtaining the calibrated airgap and iron core reluctance, their sum is namely the total calibrated reluctance, which is shown as

$$R_{\mathrm{Cali}} = R_{\mathrm{g,Cali}} + R_{\mathrm{i,Cali}}. \tag{20}$$

Finally, the final calibrated flux linkage can be calculated by

$$\psi_{\mathrm{Cali}} = \frac{N^2 i}{R_{\mathrm{Cali}}}. \tag{21}$$

The final entire flux-linkage waveform from the proposed calibrated method is given in Fig. 12.

The calibration process can be concluded as follows:

1) calibrate $R_{\mathrm{g,Cali.}}(\theta)$ in regions I and III with (16) and (17);
2) calculate coefficients a and h with (13) and (14), and calibrate $R_{\mathrm{g,Cali.}}(\theta)$ in region II with (15);
3) calculate $R_{\mathrm{i,Cali.}}$ with (19) for all current levels;
4) calculate $R_{\mathrm{g,Cali.}}$ and ψ_{Cali} with (20) and (21).

IV. Evaluation With the Experiment

To verify the feasibility and accuracy of the proposed method, the calibrated results should be compared with those from the experiment in detail. Both static and dynamic experimental results are compared in this section.

A. Evaluation With Static Measurement

Fig. 13 compares the entire flux-linkage characteristics obtained by the proposed calibrated method, FEM simulation, and the measurement method in [10]. Good agreements can be found in general except data at an extremely high current level at unaligned position. These errors could be caused by the inaccurate measurement in [10].

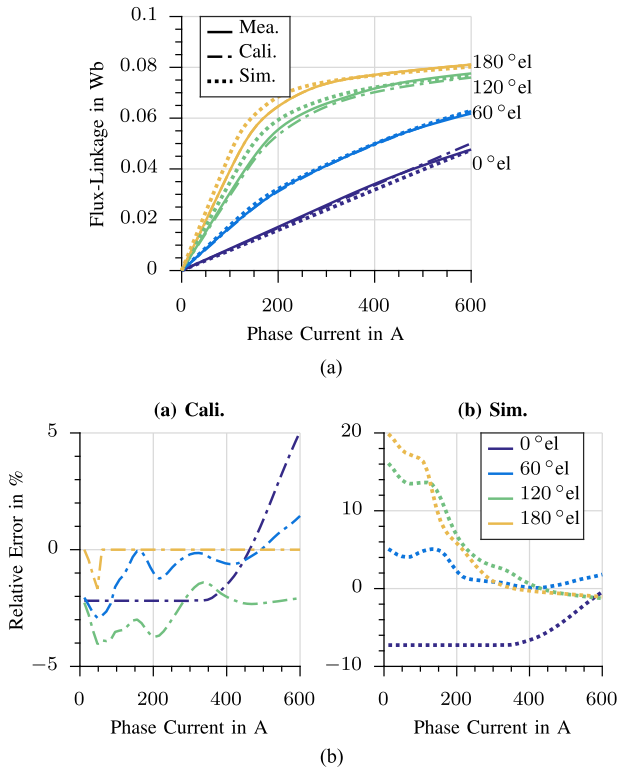

Fig. 13. Flux-linkage characteristics comparisons between the measured, calibrated, and simulated data. (a) Flux-linkage characteristics. (b) Relative errors.

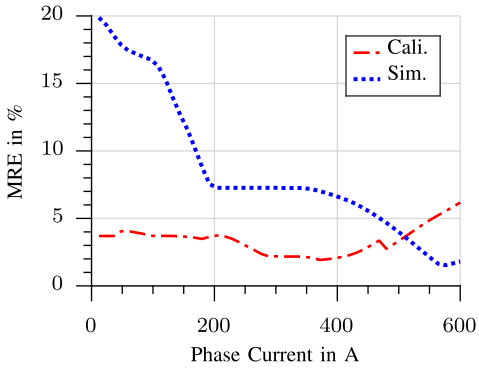

Fig. 14. MRE comparison between FEM simulation and calibrated data.

To quantitatively evaluate the accuracy of the proposed calibrated calculation method in detail, the maximum relative error (MRE) is adopted, which is defined in (22). In this paper, the FEM simulation and calibrated data are regarded as the estimated data, and the measurement data are the actual data. The MRE comparison results of the FEM simulation and the proposed calibrated method are given in Fig. 14. The accuracy of FEM simulation results is unsatisfactory, especially at low current levels. Through calibration, the accuracy has been significantly improved. The vast majority of MREs are less than 5%, and the biggest one is about 6%

$$\mathrm{MRE} = \max_{\theta=0^{\circ}\mathrm{el}}^{180^{\circ}\mathrm{el}} \left| \frac{\psi_{\mathrm{e}} - \psi_{\mathrm{a}}}{\psi_{\mathrm{a}}} \right| \tag{22}$$

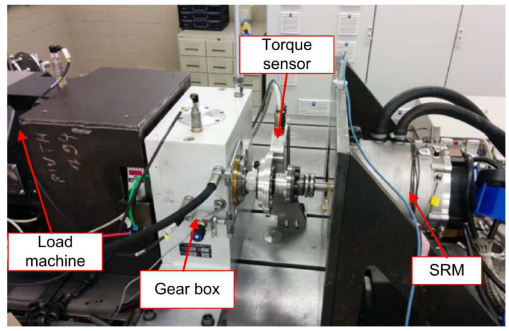

Fig. 15. Photograph of the experimental platform [15].

where ψ_{e} and ψ_{a} are the estimated and actual flux-linkage values, respectively.

B. Evaluation With Dynamic Performance

The static measurement results can evaluate flux-linkage characteristics at all current and position levels, but measurement itself has inevitable errors. To more comprehensively verify the proposed calibrated method, it should be further verified with dynamic performances. Fig. 15 shows the photograph of the experimental platform. The machine is measured and simulated for three operating points at different speeds and control strategies. These simulations are performed in MATLAB/Simulink. For each operation point, three simulations are performed with the measured, original FEM simulation, and calibrated data, respectively. The corresponding dynamic waveforms of phase current are given in Fig. 16. Fig. 16(a)–(c) are operated in the single-pulse mode, and Fig. 16(d) is operated in the current-chopping mode. Compared with simulations with FEM data, the simulations with calibrated data have better agreements with measurement results at all the investigated speeds, which further verifies the feasibility and effectiveness of the proposed method.

In this paper, errors of current are relatively small except for the high speed in Fig. 16(c). Therefore, the error under this condition should be carefully considered. Fig. 17 shows the equivalent circuit of phase winding. As can be seen from this figure, the errors might come from the variation of phase resistance R_{Cu}, iron loss resistance R_{iron}, and phase inductance L. The eddy current loss is not considered in the simulation model. Therefore, R_{Cu} is underestimated compared with the measured value. The underestimation of R_{Cu} will cause that the simulated phase current is larger than the measured one.

The iron loss resistance is neglected in the simulation model. The iron loss current in Fig. 17 can be calculated by

$$\begin{aligned} i_{\mathrm{iron}} &= \frac{u - R_{\mathrm{Cu}} i_{\mathrm{tot}}}{R_{\mathrm{iron}}} \approx \frac{u}{R_{\mathrm{iron}}} \\ &\approx \begin{cases} \frac{V_{\mathrm{dc}}}{R_{\mathrm{iron}}}, & \theta_{\mathrm{on}} \le \theta < \theta_{\mathrm{free}} \\ 0, & \theta_{\mathrm{free}} \le \theta < \theta_{\mathrm{off}} \\ -\frac{V_{\mathrm{dc}}}{R_{\mathrm{iron}}}, & \theta_{\mathrm{off}} \le \theta < \theta_{\mathrm{on}} + 360^{\circ}\mathrm{el}. \end{cases} \end{aligned} \tag{23}$$

The voltage drop in the phase resistance and transistors is neglected to simplify the analysis in (23). From this equation, it can be concluded that R_{iron} results in a bigger measured phase

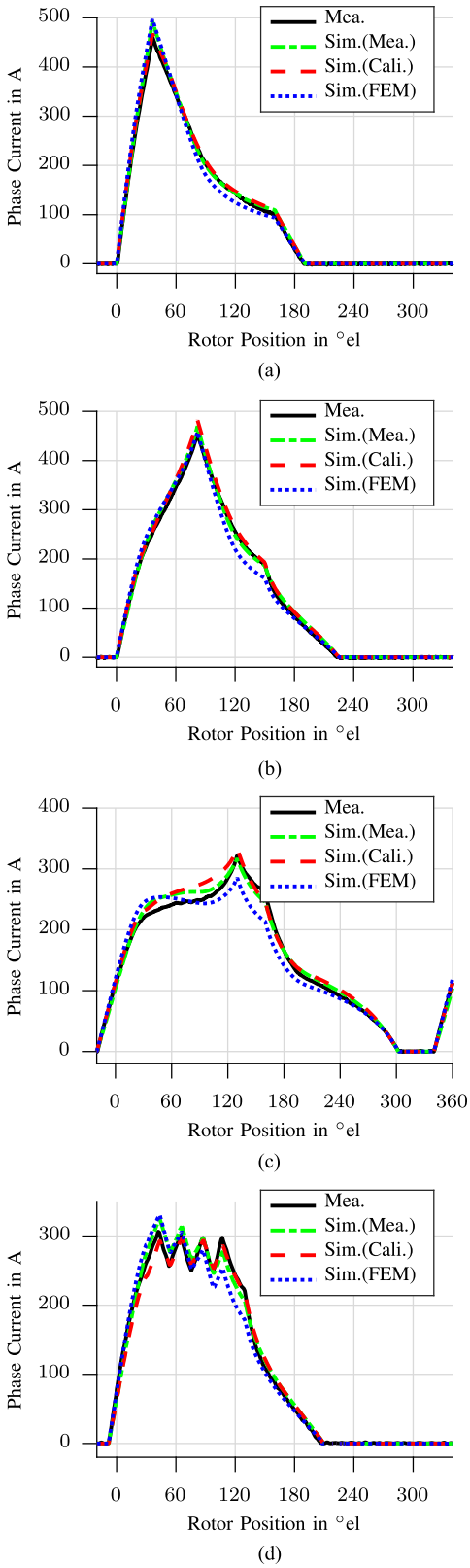

Fig. 16. Phase current waveform comparison of the dynamic simulation and experimental results. (a) $P_{\mathrm{mech}} = 19.5$ kW, $n = 3500$ r/min, $V_{\mathrm{dc}} = 345$ V, $\theta_{\mathrm{on}} = 0$ °el, $\theta_{\mathrm{free}} = 36$ °el, and $\theta_{\mathrm{off}} = 160$ °el. (b) $P_{\mathrm{mech}} = 42.9$ kW, $n = 6000$ r/min, $V_{\mathrm{dc}} = 345$ V, $\theta_{\mathrm{on}} = 0$ °el, $\theta_{\mathrm{free}} = 82$ °el, and $\theta_{\mathrm{off}} = 150$ °el. (c) $P_{\mathrm{mech}} = 53.7$ kW, $n = 10\,000$ r/min, $V_{\mathrm{dc}} = 345$ V, $\theta_{\mathrm{on}} = -20$ °el, $\theta_{\mathrm{free}} = 130$ °el, and $\theta_{\mathrm{off}} = 160$ °el. (d) $P_{\mathrm{mech}} = 34$ kW, $n = 6000$ r/min, $V_{\mathrm{dc}} = 345$ V, $\theta_{\mathrm{on}} = -8$ °el, $\theta_{\mathrm{free}} = 110$ °el, and $\theta_{\mathrm{off}} = 130$ °el.

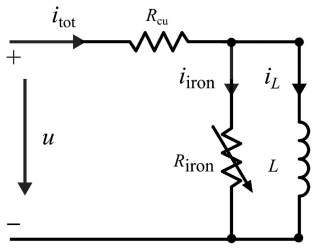

Fig. 17. Equivalent circuit of phase winding considering iron loss.

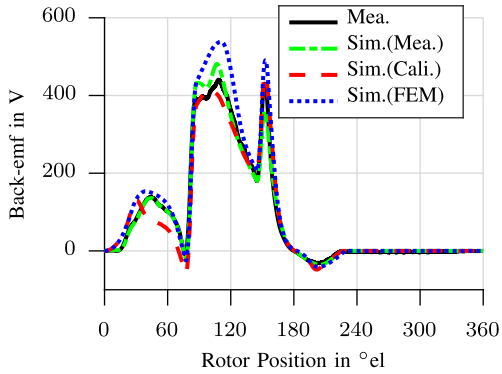

Fig. 18. Back EMF comparison of the dynamic simulation and experimental results when $P_{\mathrm{mech}} = 42.9$ kW, $n = 6000$ r/min, $V_{\mathrm{dc}} = 345$ V, $\theta_{\mathrm{on}} = 0$ °el, $\theta_{\mathrm{free}} = 82$ °el, and $\theta_{\mathrm{off}} = 150$ °el.

current value during turn-ON period and a lower value after the turn-OFF angle.

The mutual coupling is not considered in the simulation model. Due to mutual coupling between phases, the flux path in the multiphase excitation model is shorter than that in the single-phase excitation model. So, the inductance in measurement during the multiphase excitation period can be larger than the simulation model, which results in a lower current value. Similar errors can also be found in [19].

The back EMF $i\omega dL/d\theta$ is related to the rate of change in the flux linkage with respect to the rotor position, and a small variation in the flux linkage probably result in significant difference in the back EMF waveforms. In Fig. 18, the back EMF waveforms under the motoring mode from different methods are compared. It should be noted that the back EMF waveform cannot be measured directly, and it is also calculated with $i\omega dL/d\theta$ for the measurement result in Fig. 18. From the figure, a good agreement can be found between the result from the proposed method and the experiment, which is as good as that of the measurement method and better than that of FEM simulation results. This further verifies the accuracy of the flux-linkage characteristics obtained with the proposed method.

V. Discussion

To evaluate the robustness and applicability of the proposed method, the effects of some factors, such as materials, airgap length, winding placement, and SRM topologies, are discussed in this section.

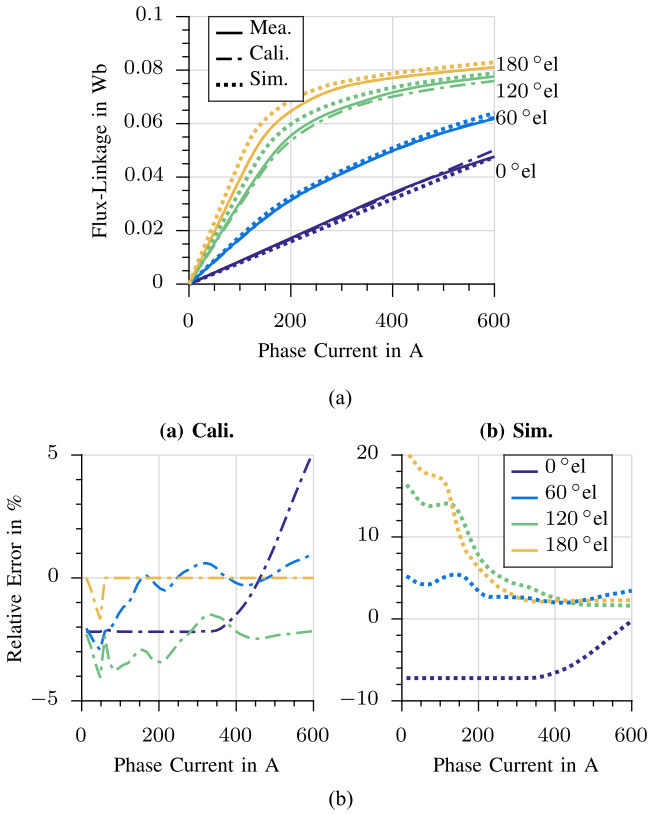

Fig. 19. Comparison of the measured, calibrated, and FEM simulated results when material is M330A. (a) Flux-linkage characteristics. (b) Relative errors.

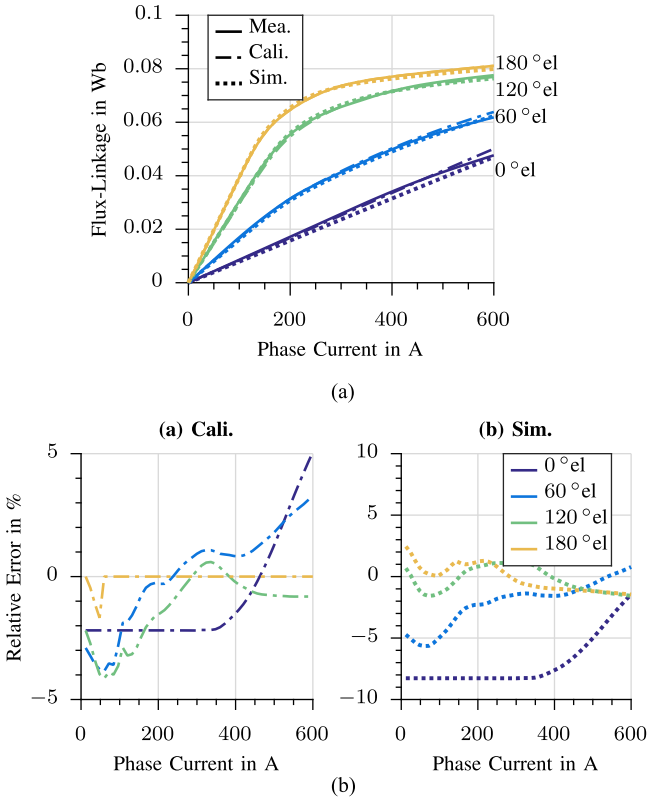

Fig. 20. Comparison of the measured, calibrated, and FEM simulated results when airgap is 0.6 mm. (a) Flux-linkage characteristics. (b) Relative errors.

A. Materials

As mentioned before, the electromagnetic properties of ferromagnetic materials will change during the process of manufacturing. In the previous section, it has been preliminarily proved that the proposed method can calibrate the change of electromagnetic properties. However, the material might be even unknown in some cases. In this section, the proposed method is further used to test the calibrated results with a wrong material (M330A). Fig. 19 compares the measured, calibrated, and FEM simulated results and the MRE with M330A. As seen in Fig. 19, the calibrated results can also match well with measured results and only slightly different with the calibrated results in Fig. 13, which indicates that the proposed method is robust with material changes.

B. Airgap

The machine electromagnetic characteristics are very sensitive to the length of airgap. The length of airgap provided by the manufacturer is 0.5 mm. However, it often has an inevitable change during the process of manufacturing and arrangement. The variation of airgap is mainly shown on the unsaturated inductance at the aligned position, which can be easily observed in Fig. 6. From (6) and (7), we can conclude that the unsaturated inductance at the aligned position is inversely proportional to airgap. Hence, the calibrated airgap can be calculated, which is 0.6 mm in this paper.

Fig. 21. Two types of winding placement. (a) Type I. (b) Type II.

Fig. 20 compares the measured, calibrated, and FEM simulated results and MRE with the calibrated airgap (0.6 mm). Both FEM simulated and calibrated results match better with measured results when the calibrated airgap is used. It can be concluded that the airgap variation plays an importance role in the final calibrated results. To achieve better calibrated results, the airgap should be calibrated first.

C. Winding Placement

For the high-speed application, winding placement can be one of uncertain factors in the FEM simulation, because the slot has to leave enough space from the airgap to reduce eddy copper losses, and researchers usually cannot get exact placement information. Fig. 21 shows two different types of winding placement. Type I is 2.45 mm to airgap, which is the one adopted in the previous simulations, and type II is 12.45 mm to airgap. The relative permeability of copper is slightly smaller than that of air, which causes the airgap reluctance (the copper reluctance is

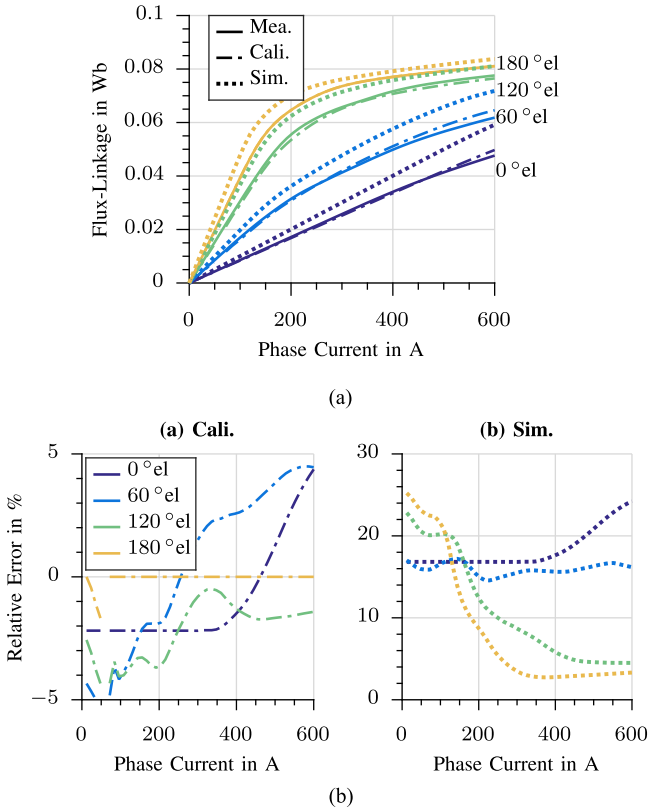

Fig. 22. Comparison of the measured, calibrated, and FEM simulated results when the winding is 12.45 mm to the airgap. (a) Flux-linkage characteristics. (b) Relative errors.

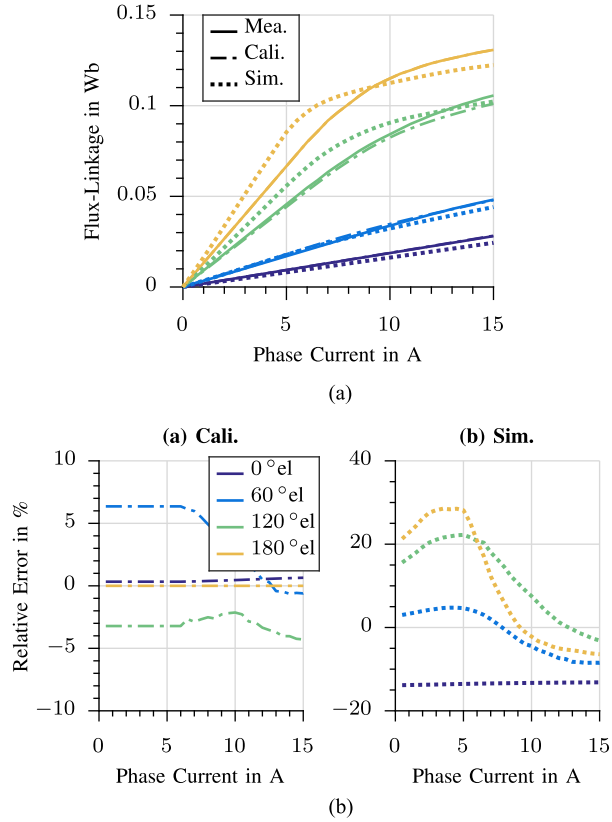

Fig. 23. Flux-linkage characteristics comparisons between the measured, calibrated, and simulated data. (a) Flux-linkage characteristics. (b) Relative errors.

equivalent to the airgap reluctance in this paper) of type II to be smaller than that of type I. Therefore, type II machine has higher inductance and flux linkage. These effects can be more clearly observed at the unaligned position, where most of the flux flows through the slides of the stator pole. The calibrated results of type II are given in Fig. 22. Though winding placement changes the flux linkage a lot, the calibrated results can still match the experiment results very well.

D. SRM Topologies

There are several topologies of SRM differentiated by phase number and combinations of the stator and rotor poles. The applicability of the proposed method to different SRM topologies should be discussed.

The measurement of flux-linkage characteristics at aligned and unaligned positions is the basis of the proposed method. For all kinds of machines, the rotor will rotate to the aligned position with high current pulses. Then, the flux-linkage characteristics can be measured by the pulse dc voltage injection. The estimation of unsaturated inductance at the unaligned position is performed through the analysis of dynamic voltage and current waveforms. It does not rely on the machine structure, either.

Theoretically, the proposed calibration method can reduce the errors uncertain factors of FEM simulations caused by the airgap, material properties, and winding placement changes during the manufacturing for all kinds of machines. During the theoretical derivation, the topologies of the SRM are not specified. As an example, Fig. 23 shows the comparison of the simulated, calibrated, and measured flux-linkage samples results of a 1-kW three-phase 12/8-pole SRM laboratory prototype [9]. The machine data are provided by a manufacturer, which is shown as SRM2 in the Appendix. From Fig. 23, it can be seen that the FEM cannot always get a good result. The MRE of flux-linkage samples is about 30%. However, good agreements are achieved after calibration, which further validate the effectiveness and applicability of the proposed method.

Nevertheless, the proposed method is not applicable for the machine with an asymmetrical structure, such as the two-phase SRM with asymmetric rotor poles in [20]. In this case, the inductance curve is also asymmetrical, and the proposed method cannot describe the reluctance model. Besides, for the machines with the short flux path and high mutual inductance, it is possible to get the flux-linkage characteristics with the proposed method, but the prediction of phase current may be not accurate.

VI. Conclusion

This paper proposed a new reluctance calibration method to calibrate the FEM simulation results with partial measurement results. It can effectively obtain the flux-linkage characteristics of the SRM on the standard test bench and has certain robustness to the variation of simulation parameters. Except the geometric dimensions, only the flux-linkage characteristics of the SRM at

aligned and unaligned rotor positions are required, which can be conveniently measured. The proposed method is simple, fast, and accurate and does not need special test bench, which reduces the cost and complexity and makes it convenient and suitable for practical applications.

APPENDIX

The ratings and parameters of the SRM prototypes are listed as follows.

TABLE I
MACHINE DATA

Symbol	Quantity	SRM1	SRM2
P_{n}	Rated power	35 kW	1 kW
$n_{\max}$	Maximum speed	23 000 r/min	8000 r/min
n_{b}	Base speed	6000 r/min	2000 r/min
N_{ph}	Number of phase	3	3
N_{s}	Number of stator	18	12
N_{r}	Number of rotor	12	8
N_{w}	Number of turns	25	119
L_{stk}	Stack length	120 mm	81 mm
D_{s}	Stator diameter	204 mm	120 mm
w_{sp}	Stator pole width	12.79 mm	8.22 mm
h_{sy}	Stator yoke height	15 mm	9.5 mm
D_{r}	Rotor diameter	135 mm	62.7 mm
w_{rp}	Rotor pole width	15.77 mm	9.26 mm
h_{ry}	Rotor yoke height	11 mm	8.85 mm
l_{g}	Airgap length	0.5 mm	0.15 mm
β_{s}	Stator pole arc	10.8°	15°
β_{r}	Rotor pole arc	13.4°	17°

REFERENCES

[1] W. Ding, S. Yang, Y. Hu, S. Li, T. Wang, and Z. Yin, "Design consideration and evaluation of a 12/8 high-torque modular-stator hybrid excitation switched reluctance machine for EV applications," *IEEE Trans. Ind. Electron.*, vol. 64, no. 12, pp. 9221–9232, Dec. 2017, doi: 10.1109/TIE.2017.2711574.

[2] H. Li, B. Bilgin, and A. Emadi, "An improved torque sharing function for torque ripple reduction in switched reluctance machines," *IEEE Trans. Power Electron.*, vol. 34, no. 2, pp. 1635–1644, Feb. 2019, doi: 10.1109/TPEL.2018.2835773.

[3] A. Chiba, K. Kiyota, N. Hoshi, M. Takemoto, and S. Ogasawara, "Development of a rare-earth-free SR motor with high torque density for hybrid vehicles," *IEEE Trans. Energy Convers.*, vol. 30, no. 1, pp. 175–182, Mar. 2015, doi: 10.1109/TEC.2014.2343962.

[4] H. Chen, W. Yan, L. Chen, M. Sun, and Z. Liu, "Analytical polynomial models of nonlinear magnetic flux linkage for SRM," *IEEE Trans. Appl. Supercond.*, vol. 28, no. 3, Apr. 2018, Art. no. 5205307, doi: 10.1109/TASC.2018.2806913.

[5] S. Yao and W. Zhang, "A simple strategy for parameters identification of SRM direct instantaneous torque control," *IEEE Trans. Power Electron.*, vol. 33, no. 4, pp. 3622–3630, Apr. 2018, doi: 10.1109/TPEL.2017.2710137.

[6] C. E. Carstensen, N. H. Fuengwarodsakul, and R. W. De Doncker, "Flux linkage determination for correct modeling of switched reluctance machines—Dynamic measurement versus static computation," in *Proc. IEEE Int. Electr. Mach. Drives Conf.*, May 2007, vol. 2, pp. 1317–1323, doi: 10.1109/IEMDC.2007.383620.

[7] A. Ferrero, A. Raciti, and C. Urzi, "An indirect test method for the characterization of variable reluctance motors," *IEEE Trans. Instrum. Meas.*, vol. 42, no. 6, pp. 1020–1025, Dec. 1993, doi: 10.1109/19.245656.

[8] K. Lu, P. O. Rasmussen, and A. E. Ritchie, "Investigation of flux-linkage profile measurement methods for switched-reluctance motors and permanent-magnet motors," *IEEE Trans. Instrum. Meas.*, vol. 58, no. 9, pp. 3191–3198, Sep. 2009, doi: 10.1109/TIM.2009.2017154.

[9] S. Song, L. Ge, S. Ma, M. Zhang, and L. Wang, "Accurate measurement and detailed evaluation of static electromagnetic characteristics of switched reluctance machines," *IEEE Trans. Instrum. Meas.*, vol. 64, no. 3, pp. 704–714, Mar. 2015, doi: 10.1109/TIM.2014.2358132.

[10] A. Hofmann, A. Klein-Hessling, I. Ralev, and R. W. De Doncker, "Measuring SRM profiles including radial force on a standard drives test bench," in *Proc. IEEE Int. Elect. Mach. Drives Conf.*, May 2015, pp. 383–390, doi: 10.1109/IEMDC.2015.7409088.

[11] L. Shen, J. Wu, S. Yang, and X. Huang, "Fast flux linkage measurement for switched reluctance motors excluding rotor clamping devices and position sensors," *IEEE Trans. Instrum. Meas.*, vol. 62, no. 1, pp. 185–191, Jan. 2013, doi: 10.1109/TIM.2012.2212598.

[12] S. Song, M. Zhang, and L. Ge, "A new fast method for obtaining flux-linkage characteristics of SRM," *IEEE Trans. Ind. Electron.*, vol. 62, no. 7, pp. 4105–4117, Jul. 2015, doi: 10.1109/TIE.2015.2390147.

[13] S. Song, L. Ge, and M. Zhang, "Data-reconstruction-based modeling of SRM with few flux-linkage samples from torque-balanced measurement," *IEEE Trans. Energy Convers.*, vol. 31, no. 2, pp. 424–435, Jun. 2016, doi: 10.1109/TEC.2016.2517924.

[14] S. Song, S. Chen, and W. Liu, "Analytical rotor position estimation for SRM based on scaling of reluctance characteristics from torque-balanced measurement," *IEEE Trans. Ind. Electron.*, vol. 64, no. 5, pp. 3524–3536, May 2017, doi: 10.1109/TIE.2016.2645144.

[15] I. Ralev, F. Qi, B. Burkhart, A. Klein-Hessling, and R. W. De Doncker, "Impact of smooth torque control on the efficiency of a high-speed automotive switched reluctance drive," *IEEE Trans. Ind. Appl.*, vol. 53, no. 6, pp. 5509–5517, Nov. 2017, doi: 10.1109/TIA.2017.2743680.

[16] S. Mao, D. Dorrell, and M. Tsai, "Fast analytical determination of aligned and unaligned flux linkage in switched reluctance motors based on a magnetic circuit model," *IEEE Trans. Magn.*, vol. 45, no. 7, pp. 2935–2942, Jul. 2009, doi: 10.1109/TMAG.2009.2016087.

[17] C. L. Xia, M. Xue, and T. N. Shi, "A new rapid nonlinear simulation method for switched reluctance motors," *IEEE Trans. Energy Convers.*, vol. 24, no. 3, pp. 578–586, Sep. 2009, doi: 10.1109/TEC.2009.2016131.

[18] B. Parreira, S. Rafael, A. J. Pires, and P. J. C. Branco, "Obtaining the magnetic characteristics of an 8/6 switched reluctance machine: From FEM analysis to the experimental tests," *IEEE Trans. Ind. Electron.*, vol. 52, no. 6, pp. 1635–1643, Dec. 2005, doi: 10.1109/TIE.2005.858709.

[19] W. Ding, D. Liang, and H. Sui, "Dynamic modeling and performance prediction for dual-channel switched reluctance machine considering mutual coupling," *IEEE Trans. Magn.*, vol. 46, no. 9, pp. 3652–3663, Sep. 2010, doi: 10.1109/TMAG.2010.2045390.

[20] D. Aliamkin, A. Anuchin, M. Lashkevich, and F. Briz, "Sensorless control of two-phase switched reluctance drive in the whole speed range," in *Proc. 42nd Annu. Conf. IEEE Ind. Electron. Soc.*, Oct. 2016, pp. 2917–2922, doi: 10.1109/IECON.2016.7793719.

Lefei Ge (S'18) was born in China in 1992. He received the B.S. degree in measurement and control technology and the M.S. degree in electrical engineering from Northwestern Polytechnical University, Xi'an, China, in 2013 and 2016, respectively. He is currently working toward the Ph.D. degree with RWTH Aachen University, Aachen, Germany.

Since September 2016, he has been a Research Associate with the Institute of Power Electronics and Electrical Drives, RWTH Aachen University. His research interests include optimal design and control of switched reluctance machines.

Iliya Ralev was born in Bulgaria in 1983. He received the Diploma and Ph.D. degrees in electrical engineering from RWTH Aachen University, Aachen, Germany, in 2012 and 2019, respectively.

Since 2013, he has been a Research Associate with the Institute of Power Electronics and Electrical Drives, RWTH Aachen University. His research interests include the control of rotating field machines and switched reluctance machines.

Annegret Klein-Hessling (S'13) was born in Germany in 1986. She received the Diploma degrees in electrical engineering and industrial engineering and the Ph.D. degree in electrical engineering from RWTH Aachen University, Aachen, Germany, in 2012 and 2018, respectively.

In October 2012, she became a Research Associate with the Institute of Power Electronics and Electrical Drives, RWTH Aachen University, where she has been a Chief Engineer since 2018. Her research interests include the field of electrical drives, in particular switched reluctance drives and their control.

Shoujun Song (M'08–SM'16) received the B.S. and M.S. degrees from Northwestern Polytechnical University, Xi'an, China, in 2003 and 2006, respectively, and the Dr.-Ing. degree from the Technical University of Berlin, Berlin, Germany, in 2009, all in electrical engineering.

He is currently an Associate Professor with the Department of Electrical Engineering, Northwestern Polytechnical University. His research interests include electrical machines and drives with an emphasis on switched reluctance machines and permanent magnet machines.

Rik W. De Doncker (F'01) received the Ph.D. degree in electrical engineering from Katholieke Universiteit Leuven, Leuven, Belgium, in 1986.

In 1987, he joined the University of Wisconsin, Madison, WI, USA, as a Visiting Associate Professor. After a short stay as an Adjunct Researcher with the Interuniversity Microelectronics Centre, Leuven, in 1989, he joined, the Corporate Research and Development Center, General Electric Company, Schenectady, NY, USA. In 1994, he joined Silicon Power Corporation, Malvern, PA, USA, a former division of General Electric Inc., as the Vice President of Technology. In 1996, he became a Professor with RWTH Aachen University, Aachen, Germany, where he currently leads the Institute for Power Electronics and Electrical Drives. Since 2006, he has been the Director of the E.ON Energy Research Center, RWTH Aachen University.

Dr. De Doncker was the President of the IEEE Power Electronics Society (PELS) in 2005 and 2006. He was the founding Chairman of the German IEEE Industry Applications Society–PELS Joint Chapter. He received the IEEE Power and Energy Society Nari Hingorani Custom Power Award in 2008 and the IEEE William E. Newell Power Electronics Award in 2013. In 2009, he led a Verband der Elektrotechnik, Elektronik, und Informationstechnik/Energietechnische Gesellschaft Task Force on Electric Vehicles. In 2010, he received an honorary doctor degree from Riga Technical University, Riga, Latvia.